Journal of
Ceramic Science
and Technology

J. Ceram. Sci. Technol., **09** [2] 101-118 (2018)
DOI: 10.4416/JCST2017-00084
available online at: http://www.ceramic-science.com
© 2018 Göller Verlag

Room-Temperature Mechanochemical Synthesis and Consolidation of Nanocrystalline HfB_2-HfO_2 Composite Powders

N. Akçamlı*[1, 2], D. Ağaoğulları[1], Ö. Balcı[3], M. L. Öveçoğlu[1], İ. Duman[1]

[1]Istanbul Technical University, Faculty of Chemical and Metallurgical Engineering, Department of Metallurgical and Materials Engineering, Particulate Materials Laboratories (PML), 34469 Maslak, Istanbul, Turkey
[2]Bursa Technical University, Faculty of Natural Sciences, Architecture and Engineering, Department of Metallurgical and Materials Engineering, Yıldırım 16330, Bursa, Turkey
[3]Koç University, Department of Chemistry, Rumelifeneri Yolu, 34450 Sarıyer, Istanbul, Turkey
received November 4, 2017; received in revised form January 7, 2018; accepted February 12, 2018

Abstract

This study reports on the *in-situ* preparation of HfB_2-HfO_2 composite powders at room temperature by means of mechanochemical synthesis (MCS) from $HfCl_4$-B_2O_3-Mg powder blends. The effects of milling duration and excess amounts of B_2O_3 and Mg reactants (20 and 30 wt%) on the HfB_2 formation mechanism were investigated. After MCS and purification, HfB_2, HfO_2 and $Mg_2Hf_5O_{12}$ phases were obtained. The $Mg_2Hf_5O_{12}$ phase decomposed during the annealing treatment conducted at 1000 °C under Ar flow. The as-synthesized, purified, annealed and subsequently leached powders were characterized with an X-ray diffractometer (XRD), stereomicroscope (SM), scanning electron microscope (SEM), transmission electron microscope (TEM) and particle size analyzer (PSA). The HfB_2-HfO_2 composite powders with an average particle size of 140 nm and predominantly rounded morphology were consolidated with cold pressing/pressureless sintering (PS) and spark plasma sintering (SPS) techniques. The relative density values of the HfB_2-HfO_2 composites obtained by means of PS (with 2 wt% Co) and SPS techniques were 91.82 % and 93.79 %, respectively. A relatively high densification rate for the HfB_2-HfO_2 ceramic was achieved by means of Co addition, which was considered a promising sintering aid for HfB_2-based ceramics. The HfB_2-HfO_2 composite sample consolidated with SPS exhibited hardness, wear volume loss amount and friction coefficient values of 18.45 GPa, 4.30 mm^3 and 0.60, respectively.

Keywords: HfB_2-HfO_2 composites, powders, solid state reaction, sintering, microstructure-final, mechanical properties

I. Introduction

Systematic research efforts have been invested in the *in-situ* preparation of ceramic composite powders over the last couple of decades. Hybrid composite materials in which the properties of each constituent are combined in one structure may provide novel applications and solutions for key industries [1–6]. For instance, ZrB_2-ZrO_2 ceramic composites have been investigated because of their stress-induced phase transformation toughening mechanism [4]. Additionally, TiB_2-TiO_2 ceramic composites have been studied for their enhanced mechanical properties and potential catalytic activity [7, 8]. Similar to these IVB group transition metals, Hf can provide improved properties in the combination of its boride and oxide compounds.

In addition to a very high melting temperature, HfB_2 exhibits high hardness, a low thermal expansion coefficient, high chemical stability, high resistance to oxidation and corrosion, high electrical and thermal conductivities. These properties make it suitable for the extreme chemical and thermal environments associated with hypersonic flights, atmospheric re-entry vehicles and rocket propulsion [9, 10]. Hf-based composites are regarded as technologically significant materials for the nuclear industry owing to the unique combination of high neutron absorption coefficient, melting point, chemical stability and mechanical properties [9–11]. Furthermore, apart from its general refractory applications, HfO_2 has been investigated as a thermal barrier coating, and its optical properties have been gaining widespread interest [12–14]. It was reported that the amount of melting during hypersonic applications has been to be found much lower in HfB_2-HfO_2 composites than in ZrB_2-based composites because of the high melting temperature of HfO_2 [15].

HfB_2 powders have been prepared predominantly with conventional borothermal and carbothermal/borothermal methods [9]. These methods generally cause particle coarsening owing to the high synthesis temperatures [9]. Nevertheless, one of the major concerns for development of material processing technology is the preparation of advanced materials and ceramics with nanocrystalline structures. Nanocrystalline materials enable significant advantages such as superior phase homogeneity, sinterability

* Corresponding author: nazli.akcamli@btu.edu.tr

and microstructure, leading to unique final mechanical properties [17, 18, 19, 20]. In recent years, some attempts have been made to prepare nano-sized HfB_2 powders with low-temperature methods like solvothermal synthesis and milling-assisted methods [21–26]. In addition, synthesis of nanocrystalline HfO_2 has been reported based on the use of sol-gel, hydrolysis of hafnium oxychloride in ethanol, and ultrasonically assisted hydrothermal treatment methods[27–31].

The highly densified HfB_2 ceramics are demanded firstly by nuclear applications that require high-neutron-absorption cross-sections and secondly by the aerospace industry[9]. Consolidation of HfB_2 powders has been investigated based on different sintering techniques [9, 10, 32, 33]. Densification of HfB_2-based ceramics with conventional techniques without external pressure or sintering additives is rather difficult because of their relatively high melting point, strong covalent bonding and low self-diffusion [32]. Two approaches are typically practiced to increase the densification rate, namely the reduction of the starting particle size and the use of sintering aids [9, 32, 33]. Recent studies have been focused on hot pressing and spark plasma sintering techniques for the consolidation of HfB_2 initial material. However, few studies detail the sintering of nano-sized HfB_2 powders (especially synthesized in laboratory facilities starting from economical reactants) and their mechanical properties [22, 23, 34].

In-situ synthesis of HfB_2-HfO_2 composite powders using a mechanochemical route as a facile and room-temperature technique, and their consolidation are the focus of the present paper. According to the best of the authors' knowledge, no work has been reported on the synthesis of HfB_2-HfO_2 composite powders by means of MCS starting from $HfCl_4$-B_2O_3-Mg blends. After MCS, annealing and purification steps, composite powders were consolidated by means of two different sintering techniques, pressureless sintering (PS with addition of 2 wt% Co) and spark plasma sintering (SPS) techniques. The physical, microstructural and mechanical properties of the bulk samples were presented based on a comparison of the sintering methods. Therefore, this study will contribute to the archival literature with the first results proposing a new method for the preparation of bulk nanostructured Hf boride-oxide ceramic composites from economical raw materials.

II. Experimental Procedure

(1) Mechanochemical synthesis, purification and annealing

In this study, HfB_2-HfO_2 composite powders were mechanochemically synthesized starting from economical raw materials, that is hafnium (IV) tetrachloride ($HfCl_4$, Alfa Aesar™, + 98 % purity), B_2O_3 (ETI Mine, 98 % purity, 421.64 μm average particle size) and Mg (MME, 99.7 % purity, 142.70 μm average particle size) powders. The initial stoichiometric $HfCl_4$-B_2O_3-Mg blends and those including excess amounts of B_2O_3 and Mg (20 and 30 wt%) were prepared according to the reaction in Eq. (1). For each run, powder batches of 6 g were weighed in a Plaslabs™ glove box under Ar (Linde™, 99.999 % purity) atmosphere and sealed in milling vials.

$$HfCl_4 + B_2O_3 + 5Mg \rightarrow HfB_2 + 3MgO + 2MgCl_2 \quad (1)$$

The powder blends were mechanochemically synthesized at room temperature in a Spex™ high-energy ball mill at 1200 rpm for different durations (up to 5 h). A hardened steel milling vial (50 ml) and balls (∅ 6 mm) were used as milling media, and the ball-to-powder weight ratio was selected as 10:1. The blends that were not subjected to the mechanochemical process were designated as-blended powders.

After milling, as-synthesized powders were purified by washing with distilled water and leaching with 4 M aqueous HCl solution (Merck™, 37 % concentrated) for the removal of $MgCl_2$ and MgO by-products, respectively. The leaching treatments were applied for 15 min with a solid-to-liquid ratio of 1 g/10 ml under the effect of ultrasonic agitation. For efficient decantation, centrifugation was applied to leaching solutions in a Hettich™ Rotofix 32A centrifuge using a rotation speed of 3500 rpm for 20 min. The residual solids were rinsed with distilled water at least three times and all the precipitation steps in centrifugation were repeated. The insoluble solids were dried in a vacuum oven (Jingke™) at 100 °C for 24 h. An annealing treatment was applied to purified powders to observe a probable phase transformation at 1000 °C with a heating and cooling rate of 10 K/min for 3 h under Ar gas flow in a Thermoscientific™ F21130 tube furnace.

(2) Consolidation of the purified powders

The purified powders were consolidated by means of cold pressing, pressureless sintering (PS), and spark plasma sintering (SPS) techniques. For the PS experiments, Co was utilized as sintering aid to achieve a higher relative density at a reduced temperature. 2 wt% Co (Alfa Aesar™, 99.5 % purity, 44 μm average particle size) was incorporated into the purified powders by means of mechanical milling for a short time (5 min) in order to obtain a homogeneous mixture. The milling parameters such as milling media, atmosphere and ball-to-powder weight ratio were the same as those employed during the MCS process. The Co-incorporated HfB_2-HfO_2 powders were compacted by means of cold pressing (CP) in a 10-tonne capacity MSE™ MP-0710 uniaxial hydraulic press under a pressure of 800 MPa to obtain cylindrical specimens (∅ 6.3 mm). These green bodies were sintered at 1500 °C for 5 h in a Linn™ HT-1800 high-temperature controlled-atmosphere furnace with a heating and cooling rate of 10 K/min under Ar atmosphere. The sintering temperature was selected with regard to the melting temperature of Co (~ 1495 °C) to enable liquid phase sintering [42]. Since the SPS technique enables increased sintering kinetics, which can be explained by the applied mechanical pressure and the high-intensity pulsed direct current passing through the powder compacts, Co aid was not utilized during SPS [23, 35]. For the SPS experiments, powders were loaded into a graphite die (∅ 20 mm) and sintered in a FCT Systeme™ HP D 25 N at 1700 °C for 15 min with a heating and cooling rate of 100 K/min under an applied holding pressure of 60 MPa.

(3) Characterization

The theoretical interpretations for the effects of excess Mg usage on the $HfCl_4$-B_2O_3-Mg system were made by utilizing FactSage™ 6.2 thermochemical software. A Bruker™ D8 Advanced Series X-ray diffractometer (XRD) with CuKα radiation (λ = 0.154 nm, 40 kV and 40 mA) in the 2θ range of 10 – 90° with a scan rate of 2°/min and a step size of 0.02° was utilized for phase analyses of the mechanochemically synthesized, purified, annealed and consolidated powders. For identifying crystalline phases, the International Center for Diffraction Data (ICDD) powder diffraction files were applied. The effect of milling duration on the crystallite size and lattice strain of HfB_2 phase was determined using a Bruker™-AXS TOPAS 4.2 software using the modified Scherrer's formula based on the broadening of the most intense XRD diffraction peaks (with (001), (100) and (101) reflections) fitted according to the Lorentzian profile by applying a fundamental parameters approach. Average crystallite size and lattice strain values were reported as the arithmetic mean of five different measurements with standard deviation. Fourier transform infrared (FTIR) analyses of the powder samples were performed in a Bruker™ Alpha-T spectrometer equipped with DRIFT module using KBr pellet technique. FTIR spectra were recorded at the wave number range of 750 – 4000 cm^{-1} in the resolution of 4 cm^{-1} with a sample/background scan time of 24 scans/min. The average particle sizes of the milled, purified and annealed powders were determined using a Microtrac™ Nano-flex particle size analyzer (PSA) equipped with a Bandelin Sonopuls™ ultrasonic homogenizer using distilled water as the aqueous media, and arithmetic means with standard deviations were calculated from three different measurements. The general images of the as-synthesized, purified and annealed powders were captured using a Zeiss™ DiscoveryV12 stereomicroscope (SM) coupled with a Zeiss™ Axiocam ERc5s high-resolution digital camera. The microstructures of the as-synthesized and purified powders were investigated by utilizing a FEI-Quanta FEG 250 scanning electron microscope (SEM) and JEOL™ JC-6000 Neoscope SEM equipped with an energy-dispersive X-ray spectrometer (EDX) using an acceleration voltage of 12 kV. For SEM analysis, the specimens were prepared by suspending the powders in C_2H_5OH (Merck™, 99.9 % purity), transferring them onto a base plate, drying them in air and coating their surfaces with a very thin layer of Au (Polaron™ SC7620 sputter coater) for ensuring electrically conductive samples. Additionally, a JEOL JEM-ARM200CFEG UHR transmission electron microscope (TEM) was utilized for obtaining bright field images and selected area electron diffraction (SAED) patterns. For TEM analysis, suspended particles were dropped on a porous carbon film which was supported on a Cu grid and dried in air.

The Archimedes densities of the consolidated samples were determined in ethanol and the results were reported as the arithmetic mean of three consecutive measurements. Standard metallographic sample preparation steps, such as hot-mounting in a Struers™ LaboPress-1, grinding and polishing in a Struers™ Tegrapol-15 instrument, were applied to the sintered samples prior to microstructural and mechanical analyses. Vickers microhardnesses of the bulk samples were measured using a Shimadzu™ HMV Microhardness Tester under a load of 200 g for 15 s. The microhardness test result of each sample contained the arithmetic mean of 25 successive indentations and standard deviation. Reciprocating sliding wear tests were conducted on the bulk samples at laboratory conditions using an alumina ball (∅ 6 mm) placed in a Tribotechnic™ Oscillating Tribotester. Applied force of 4 N, sliding speed of 6 mm/s, stroke length of 2 mm and total sliding distance of 200 000 mm were the conditions of the wear tests. Wear tracks of the sintered samples were imaged using a Hitachi™ TM-1000 SEM (operated at 15 kV) and evaluated by using a Veeco™ Dektak 6M Stylus profilometer. The wear test result for each sample in terms of wear volume loss included the arithmetic mean of three different measurements. Wear volume loss values were converted to relative wear resistance values by dividing the highest wear volume loss by the individual loss of each sample.

III. Results and Discussion

(1) Thermodynamic calculations

The molar amounts of the reactants and products varying according to the B_2O_3 and Mg amounts which were calculated for room temperature using FactSage™ thermochemical software are illustrated in Fig. 1(a) and (b), respectively. According to Fig. 1(a), when 1 mole of B_2O_3 (stoichiometric amount) participates in the reaction, HfB_2 (1 mole), MgO (3 moles) and $MgCl_2$ (2 moles) reach their maximum values. As the amount of B_2O_3 increases above 2 moles, two different kinds of Mg borate phases ($Mg_2B_2O_6$ and MgB_4O_7) occur. However, $Mg_2B_2O_5$ phase vanishes at 7 moles of B_2O_3. Simultaneously, excess B_2O_3 increases and MgB_4O_7 gets its highest molar amount. As seen in Fig. 1(b), $HfCl_4$ and B_2O_3 are completely consumed respectively at 2 and 3 moles of Mg, which indicates stepwise and individual reductions of $HfCl_4$ and B_2O_3 by Mg. HfB_2, MgO and $MgCl_2$ reach their maximum amounts with the utilization of 5 moles of Mg (stoichiometric amount) and their amounts remain constant after this value. Besides, MgB_2O_5 and HfO_2 disappear when 4 and 5 moles of Mg are used, respectively. The excess amount of Mg over 5 moles does not change the amounts of the HfB_2, MgO and $MgCl_2$, and unreacted Mg occurs in the system. On the basis of Fig. 1(a) – (b), MCS experiments should be constitutively conducted on the $HfCl_4$-B_2O_3-Mg system by using the stoichiometric amounts of B_2O_3 and Mg.

(2) Phase analyses of the mechanochemically synthesized, purified and annealed powders

Fig. 2 shows the XRD patterns of the as-blended $HfCl_4$-B_2O_3-Mg powder blends in stoichiometric amount and those mechanochemically synthesized at different durations up to 5 h. In the XRD patterns of the as-blended $HfCl_4$-B_2O_3-Mg powders and those milled for 10 min, $HfOCl_2{\cdot}4H_2O$ (ICDD Card No: 15 – 0380), $HfOCl_2{\cdot}6H_2O$ (ICDD Card No: 47 – 0816) and Mg

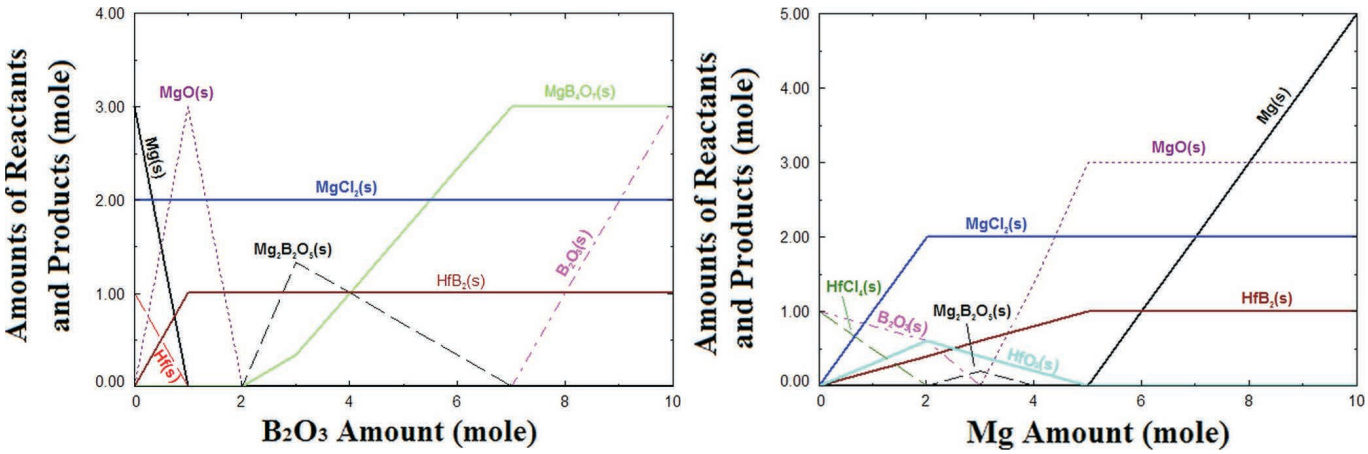

Fig. 1: Molar amounts of reactants and products varying according to the molar amounts of: (a) B_2O_3 and (b) Mg with regard to Eq. (1) at room temperature.

(ICDD Card No: 35 – 0821, Bravais Lattice: primitive hexagonal, a = b = 0.321, c = 0.521) phases were detected. $HfOCl_2.xH_2O$ compounds formed during XRD analyses which were performed under atmospheric conditions owing to the very hygroscopic character of $HfCl_4$. In addition, the B_2O_3 phase could not be determined in the XRD patterns of the as-blended $HfCl_4$-B_2O_3-Mg powder blends and those of the 10-min-milled blends because of its amorphous structure. On the other hand, after milling for 15 min, HfB_2 (ICDD Card No: 38 – 1398, Bravais lattice: primitive hexagonal, a = b = 0.314 nm, c = 0.347 nm), HfO_2 (ICDD Card No: 34 – 0104, Bravais lattice: primitive monoclinic, a = 0.528 nm, b = 0.518 nm, c = 0.511 nm, β = 99.259°), MgO (ICDD Card No: 89 – 7746, Bravais lattice: face-centered cubic, a =b =c = 0.420 nm) and $MgCl_2{\cdot}4H_2O$ (ICDD Card No:053 – 0258, Bravais lattice: primitive monoclinic, a = 0.590 nm, b = 0.727 nm, c = 0.842 nm, β = 111.007°) phases were detected in the XRD patterns. Also, an unpredicted phase, $Mg_2Hf_5O_{12}$ (ICDD Card No: 033 – 0862, Bravais lattice: primitive rhombohedral, a = b = 0.939 nm, c = 0.870 nm), was observed in the XRD patterns of the 15-min-milled powders. It can be observed from Fig. 2 that the mechanochemical reaction between the reactants starts after a relatively short milling duration of 15 min. Although the HfB_2 formed after milling for 15 min, MCS was maintained up to 5 h with the aim of observing any probable changes in the emerged phases and their peak intensities. Nevertheless, the phases detected in the XRD patterns and their peak intensities did not illustrate any obvious difference after 1 h of milling. In addition, any milling operation longer than 5 h was not applied because of possible amorphization at the prolonged milling durations.

Excess amounts of B_2O_3 and Mg were also utilized to examine the effects of reactant amounts on the mechanochemical reaction of $HfCl_4$-B_2O_3-Mg, and especially with the aim of elimination of the HfO_2 phase. The XRD patterns of the $HfCl_4$-B_2O_3-Mg powders having 30 wt% excess B_2O_3 and 30 wt% excess B_2O_3-20 wt% excess Mg after milling for 3 h are given in Fig. 3(a) and (b), respectively. After milling for 3 h, the detected phases in Fig. 3(a) and (b) were similar to those in Fig. 2. Moreover, a significant change was not observed in the distribution and intensities

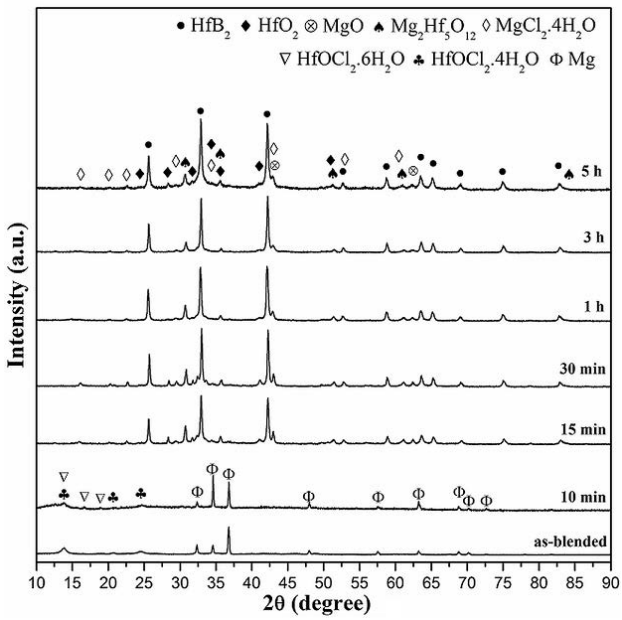

Fig. 2: XRD patterns of the as-blended $HfCl_4$-B_2O_3-Mg powder blends in stoichiometric amounts and those mechanochemically synthesized at different durations up to 5 h.

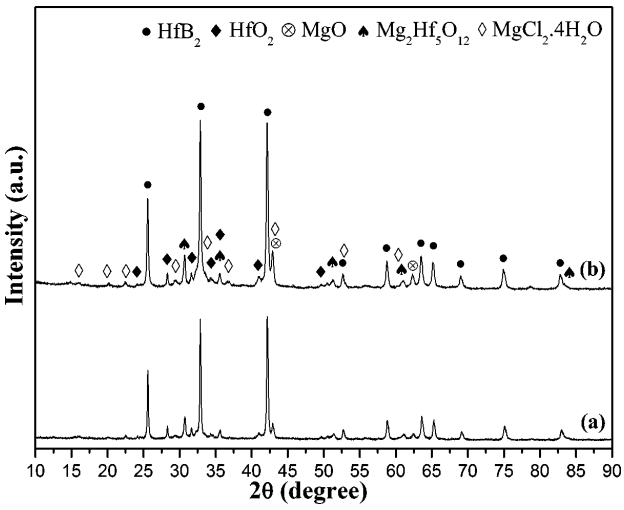

Fig. 3: XRD patterns of the $HfCl_4$-B_2O_3-Mg powders mechanochemically synthesized for 3 h using: (a) 30 wt% excess B_2O_3 and (b) 30 wt% excess B_2O_3 and 20 wt% excess Mg.

of the yielded phases with the use of excess B_2O_3 and Mg, as compatible with the thermodynamic calculations. Besides, the occurrence of HfO_2 in excess reactant amounts did not conform to Fig. 1(b) in which HfO_2 vanished with stoichiometric amount of Mg. This can be related with the unavoidable formation and stability of HfO_2 in the presence of hygroscopic chloride reactant and B_2O_3. In the XRD pattern of the as-blended and 10-min-milled powders in Fig. 2, the formation of hydrated hafnium oxychloride compounds was observed. Also, the hydroscopic behavior of $HfCl_4$ was investigated in detail in our previous study [22]. According to this study, the formation of Hf-OH bonds resulting from the reaction of $HfCl_4$ with moisture was indicated in the FTIR spectra of $HfCl_4$ and $HfCl_4$-B_2O_3-Mg powders blends[22]. Since $HfCl_4$ is highly hygroscopic, hafnium oxychloride instantly forms when it comes into contact with air. $HfOCl_2$ particles can be further hydrated up to a maximum hydration level of $HfOCl_2 \cdot 8H_2O$ [33]. Barraud *et al.* (2006) stated that partially hydrated $HfOCl_2.nH_2O$ powders consist of a $HfCl_4$ core surrounded by hydrated outer layers having different hydration rates[33]. Additionally, in previous studies on the HfB_2 synthesis which utilized $HfCl_4$ as hafnium source, the formation and stability of hafnium oxychloride was reported [21–23, 36, 37]. On the basis of Fig. 2 and 3, stoichiometric $HfCl_4$-B_2O_3-Mg powder blends were used for the subsequent experimental investigations. Experimental findings corresponded well with the Factsage^{TM} predictions (Fig. 1) and indicated that the usage of B_2O_3 and Mg over stoichiometric amounts did not affect the amounts of the desired reaction products (HfB_2, MgO and $MgCl_2$).

After the mechanochemical reaction, by-products such as $MgCl_2$ and MgO were eliminated by leaching treatments. Magnesium salts ($MgCl_2$ and $MgCl_2 \cdot 4H_2O$) were leached out by means of repeated rinsing of the powders with distilled water. Afterwards, leaching with 4 M HCl was conducted for removal of the MgO phase. XRD patterns of the stoichiometric $HfCl_4$-B_2O_3-Mg powders after MCS at different durations and subsequent purification treatments are illustrated in Fig. 4. The $MgCl_2$, $MgCl_2 \cdot 4H_2O$ and MgO phases are not observed in the XRD patterns after purification steps, proving the elimination of the undesired Mg-based phases. In the XRD patterns of 15- and 30-min-milled and -purified powders, intensities of the $Mg_2Hf_5O_{12}$ phase are higher than those of 1-, 3- and 5-h-milled and -purified powders. This indicates that the reaction is not complete, and steady-state conditions are not reached in terms of phase distributions after 30 min of MCS. The change in the intensity of $Mg_2Hf_5O_{12}$ phase with the milling duration may be explained based on some cases. At the first stage of the reduction of $HfCl_4$ particles, Mg reacts firstly with the moisture and hafnium oxychloride on the outermost layer of the hydrated $HfCl_4$ [33]. Also, it can be thought that at this stage a simultaneous formation of MgO and HfO_2 occurs and a chemical bond between HfO_2 and MgO forms, leading to the formation of $5HfO_2 \cdot 2MgO$ compound while some of the MgO (formed by reaction of Mg with moisture, $HfOCl_2.xH_2O$ and B_2O_3) remains unconfined. Besides, at longer milling durations, some of the $Mg_2Hf_5O_{12}$ phase may be broken down to form MgO and HfO_2, which results in a reduced intensity of this phase. Additionally, the intensities of $Mg_2Hf_5O_{12}$ phase in the XRD patterns of 15- and 30-min-milled powders in Fig. 2 increase after purification in the Fig. 4. At the beginning of the mechanochemical reaction, the first resulting $Mg_2Hf_5O_{12}$ phase can be in a form surrounded by amorphous phases such as B_2O_3, $HfOCl_2 \cdot 4H_2O$ and $HfOCl_2 \cdot 6H_2O$, and after rinsing and acid leaching, the intensity of $Mg_2Hf_5O_{12}$ phase increases after the removal of these amorphous phases. Moreover, the peak intensities of HfB_2, HfO_2 and $Mg_2Hf_5O_{12}$ phases do not show a very significant difference after 1 h of milling and the XRD patterns remain almost the same when the milling duration is extended to 5 h. This result indicates that the duration of MCS does not affect the types of the formed phases (between 15 min and 5 h) and after a certain time of milling (after 1 h) a steady-state reaction condition was reached.

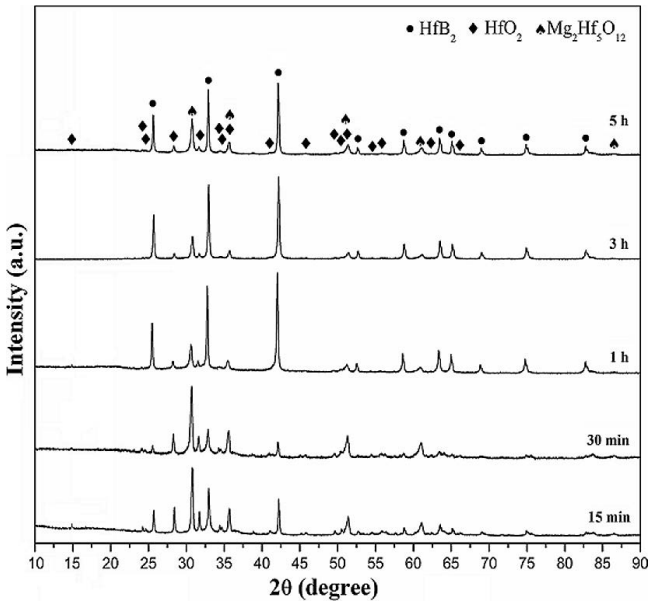

Fig. 4: XRD patterns of the stoichiometric $HfCl_4$-B_2O_3-Mg powders after mechanochemical synthesis at different durations and subsequent washing and HCl leaching treatments.

Figs. 5(a) – (c) illustrate the FTIR spectra of the commercial $HfOCl_2 \cdot 8H_2O$ powders and the stoichiometric $HfCl_4$-B_2O_3-Mg powders after MCS for 3 h and those after washing treatment, respectively. The FTIR spectrum of $HfOCl_2 \cdot 8H_2O$ powders was given with the aim of comparison. The commercial $HfOCl_2 \cdot 8H_2O$ powders show broad absorption peaks having maximum points at around 1249, 1394, 1608 and 3200 cm^{-1} (Fig. 5 (a)). It was previously shown in the literature that the broad vibration peaks between 2600 and 3650 cm^{-1} in the FTIR spectrum of a hydrated hafnium oxychloride were associated with the O-H stretching of water molecules (physically adsorbed water) while peaks at 1616 cm^{-1} were associated with their bending mode [38, 39]. Small peaks at the wave numbers of 1421, 1484, 1593 and 3460 cm^{-1} in the FTIR spectra of $HfCl_4$-B_2O_3-Mg powders after MCS for 3 h indicate the presence of compounds containing the hydroxyl group such as hafnium oxychloride hydrates ($HfOCl_2 \cdot 4H_2O$ and $HfOCl_2 \cdot 6H_2O$) and $MgCl_2 \cdot 4H_2O$

at very low amount [22, 38–40]. Moreover, it is considered that these peaks evolve inevitably because of extremely hygroscopic character of $HfCl_4$ powders. Although, all the powder preparation and milling processes were conducted under Ar atmosphere, an amount of hafnium oxychloride hydrate compounds can unavoidably form. On the other hand, the absence of the peaks belonging to the hydrated hafnium oxychloride compounds in the XRD patterns of the 3-h-milled powders (Fig. 2) indicates their lower amounts below the detection limit of the diffractometer (2 wt% of the overall sample). Additionally, after purification, there are no peaks belonging to O-H-bond-related compounds in Fig. 5(c). It should also be noted that the spectrometer is not capable of detecting a Mg-O bond. Thus, it can be said that the complete removals of $HfOCl_2{\cdot}4H_2O$, $HfOCl_2{\cdot}6H_2O$ and $MgCl_2{\cdot}4H_2O$ were achieved by the purification treatments.

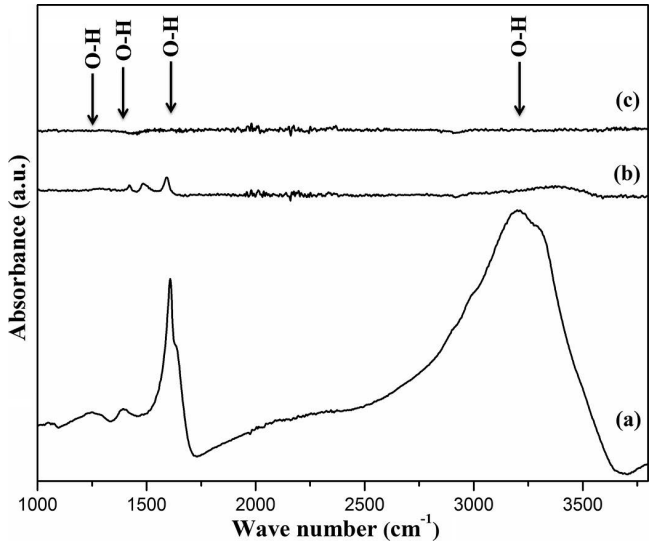

Fig. 5: FTIR spectra of the commercial $HfOCl_2{\cdot}8H_2O$ powders (a), the stoichiometric $HfCl_4$-B_2O_3-Mg powders after mechanochemical synthesis for 3 h (b) and subsequent washing and leaching treatments (c).

An annealing treatment was applied to the mechanochemically synthesized powders after purification with the aim of investigating any possible decomposition or transformation of the present phases. The products obtained after 3 h of MCS of the stoichiometric $HfCl_4$-B_2O_3-Mg powders and subsequent purification treatments (with distilled water and 4 M HCl) were annealed at 1000 °C for 3 h. Fig. 6(a) illustrates the XRD pattern of the annealed powders. After the annealing treatment, the only phases detected in the XRD patterns were HfB_2 and HfO_2, whereas the $Mg_2Hf_5O_{12}$ phase was not observed. It is considered that during the annealing, the $Mg_2Hf_5O_{12}$ phase (contains 7.11 wt% of MgO) decomposed into the HfO_2 and MgO phases upon heating. $Mg_2Hf_5O_{12}$ phase is shown in the HfO_2-MgO binary phase diagram at 28.57 % molar amount of MgO and its stability range is stated as 1370–2348 °C [41]. However, there is no detailed information about the $Mg_2Hf_5O_{12}$ phase in the literature although its formation was reported in our previous study on the autoclave processing of the $HfCl_4$-B_2O_3-Mg system at 500 °C for 12 h [22]. In the same study, it was determined that the $Mg_2Hf_5O_{12}$ phase was decomposed into HfO_2 and MgO phases during the sintering process conducted at 1700 °C [22]. This new finding indicated that the $Mg_2Hf_5O_{12}$ phase is also not stable at/above 1000 °C for long holding durations even though a higher stability range over this temperature is given in the HfO_2-MgO binary phase diagram [41]. This can be derived from the differences in the formation mechanisms of $Mg_2Hf_5O_{12}$ during various processes. Nevertheless, in the XRD patterns after annealing, the MgO phase was not observed (Fig. 6(a)), which could be explained by its low amount under the detection limit of the equipment. Samad *et al.* reported that the $Mg_2Zr_5O_{12}$ phase, which formed via thermally sprayed coatings of ZrO_2-24 wt% MgO, decomposed to MgO and ZrO_2 phases during hot isostatic pressing at 1100 °C [42]. Moreover, the increase in the peak intensities of the HfO_2 phase after the annealing could be explained by the formation of additional amount of HfO_2 by the decomposition of $Mg_2Hf_5O_{12}$. A leaching treatment with 4 M HCl was applied to the annealed powders for the elimination of any probable MgO impurity. The XRD patterns of these powders are given in Fig. 6(b). Any significant difference between the XRD patterns of the annealed and additionally HCl-leached powders was not determined as clearly seen from Fig. 6(a) and (b).

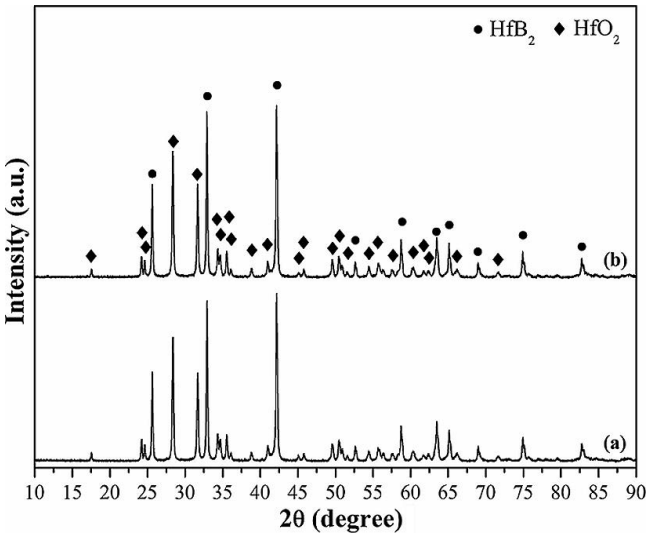

Fig. 6: XRD patterns of the 3 h of mechanochemically synthesized and purified stoichiometric $HfCl_4$-B_2O_3-Mg powders after: (a) annealing at 1000 °C for 3 h and (b) subsequent HCl leaching.

The semi-quantitative phase analyses of the mechanochemically synthesized and purified powders and those annealed and leached ones were conducted with the Rietveld refinement method based on their XRD patterns in Fig. 4 and 6(b) in order to determine the amounts of HfB_2 phase. According to the Rietveld analysis results in Table 1, the HfB_2 amounts in the 1-, 3- and 5-h mechanochemically synthesized and purified powders were determined as 52.8, 53.4 and 52.4 wt%, respectively. The increasing milling duration did not lead to any notable change in the amount of HfB_2 phase. However, a consistency in the amount of the major phase was obtained. It was thought that slight differences in the amounts of the evolved phases might be observed in the MCS process, which was caused

Table 1: Semi-quantitative phase analysis results of the mechanochemically synthesized and purified powders and the annealed and leached powders based on the Rietveld refinement method.

Sample	HfB_2 Amount (wt%)
MCS for 1 h and purified	52.8
MCS for 3 h and purified	53.4
MCS for 5 h and purified	52.4
MCS for 3 h, annealed and leached	57.2

by the incidental conditions of this particular method such as different distribution of the reactant particles in the different regions and interaction between them until steady-state conditions were reached [17, 35]. Therefore, it can be said that the system reached a steady-state condition after the milling duration of 1 h. Additionally, the HfB_2 amount after annealing and leaching treatments was determined as 57.2 wt%. After the removal of MgO phase evolved by the decomposition of $Mg_2Hf_5O_{12}$ phase during the annealing at 1000 °C, an increase in the HfB_2 amount was observed.

(3) Microstructural analyses of the mechanochemically synthesized, purified and annealed powders

SM images of the stoichiometric as-blended $HfCl_4$-B_2O_3-Mg powders and those mechanochemically synthesized, purified and annealed ones are illustrated in Fig. 7(a) to (g). The SM images of the powders throughout the MCS process could give a general idea about the progress of the intended reactions. As seen from Fig. 7(a), the as-blended $HfCl_4$-B_2O_3-Mg powders included reactant powders with relatively different particle sizes and illustrated a non-uniform appearance. Moreover, color of the as-blended powders indicated only a physical mixing (Fig. 7(a)) instead of a well-distributed form obtained after MCS for 10 min (Fig. 7(b)). On the other hand, with the increase of milling duration to 15 min, the color of $HfCl_4$-B_2O_3-Mg powders turned to dark gray, which indicated the formation of new chemical species different from the starting ones (Fig. 7(c)). These observations are in good accordance with the XRD findings in Fig. 2 in which the formation of HfB_2 phase was determined to start after MCS for 15 min. Fig. 7(d) and (e) show the SM images of the $HfCl_4$-B_2O_3-Mg powders after 3 and 5 h of MCS, respectively. The lighter or shiny phases between the dark gray powders in Figs. 7(c), (d) and (e) might be Mg-based by-products. After the subsequent purifications with distilled water and 4 M HCl, the mechanochemically synthesized powders gained a homogeneous appearance (Fig. 7(f)) without an indication of shiny particles. No particular change in the appearance of the powders was observed after MCS for 3 h, purification and annealing (Fig. 7(g)), which may also be interpreted as an evidence for the structural stability of the desired phases.

A secondary electron SEM image of the stoichiometric $HfCl_4$-B_2O_3-Mg powders after MCS for 3 h and purification is displayed in Fig. 8(a). As seen from figure, purified powders consisted of round-shaped particles with sizes below 250 nm. Additionally, SEM/EDS/EDX analyses were conducted on the stoichiometric $HfCl_4$-B_2O_3-Mg powders after MCS for 3 h and purification Fig. 8(b) – (h). The only detected elements in these analyses are Hf, O, B and Mg. Likewise, it can be said that the Cl exists only in a trace amount, such as residual contamination. Additionally, the phase distribution of the purified powders was investigated with elemental mapping analyses. Fig. 8(d) – (g) represents the corresponding elemental Hf, O, B and Mg maps taken from the SEM image in Fig. 8(b). A homogeneous distribution of Hf, O, B and Mg is seen throughout the microstructure in Fig. 8(d) – (g). Owing to the very high phase homogeneity and composite character of the synthesized powders, Hf, O, B and Mg elements give very close signals throughout the microstructure on the EDX mapping analysis. The results confirm that the mechanochemical synthesis technique provides superior size uniformity and homogeneous distribution of the phases. In addition, in order to show the correlation between the O and Hf and homogeneous distribution of Hf, O, B and Mg throughout the microstructure, a mapping with overlapped signals was added as shown in Fig. 8(h). The removal of MgO phase formed via the magnesiothermic reduction reactions during the MCS of boride compounds is a well-known process and shown in the previous studies [22, 43, 44]. Accordingly, the existence of Mg even after 4 M HCl leaching arose from the presence of $Mg_2Hf_5O_{12}$ phase, which was also detected in the XRD analysis of the purified powders in Fig. 3. Therefore, the elemental maps confirmed the formation of HfB_2, HfO_2 and $Mg_2Hf_5O_{12}$ phases and also their uniform distribution throughout the microstructure.

Figs. 9(a) through (h) illustrate the secondary electron SEM/EDS/EDX analyses of the powders synthesized by means of mechanochemical synthesis for 3 h, purification, annealing and additional leaching treatments. In the SEM images (in Figs. 9(a) and (b)), powders having round-shaped morphology and particle size under 250 nm can be observed, and they gain a more uniform and close-sized appearance after the annealing and additional purification treatment by elimination of $Mg_2Hf_5O_{12}$ phase. The line at approximately 1.3 keV in the EDS spectra shown in the Fig. 9(c) is an overlapped peak for Hf and Mg, as formerly seen in the EDS analysis of the purified powders (in Fig. 8(c)), and it is very difficult to differentiate them because of this mutual peak interference. Nevertheless, the peak intensity at 1.3 keV after annealing and leaching treatments slightly decreased, which can be attributed to the elimination of the Mg-containing phase. In the XRD pattern of mechanochemically synthesized, annealed and leached powders (Fig. 6), the $Mg_2Hf_5O_{12}$ phase was not found, which was ascribed to the decomposition of this phase. Moreover, it is a well-known procedure to eliminate MgO phase by means of HCl leaching. Therefore, it can be asserted that the peak at around 1.3 keV comes from the Hf signal. Moreover, the distribution of Hf, O and B was illustrated in the mapping analyses (in Figs. 9(d) – (g)), after elimination of Mg-containing phase. According to these mappings, it can be said that the synthesized powders show high phase homogeneity and composite character.

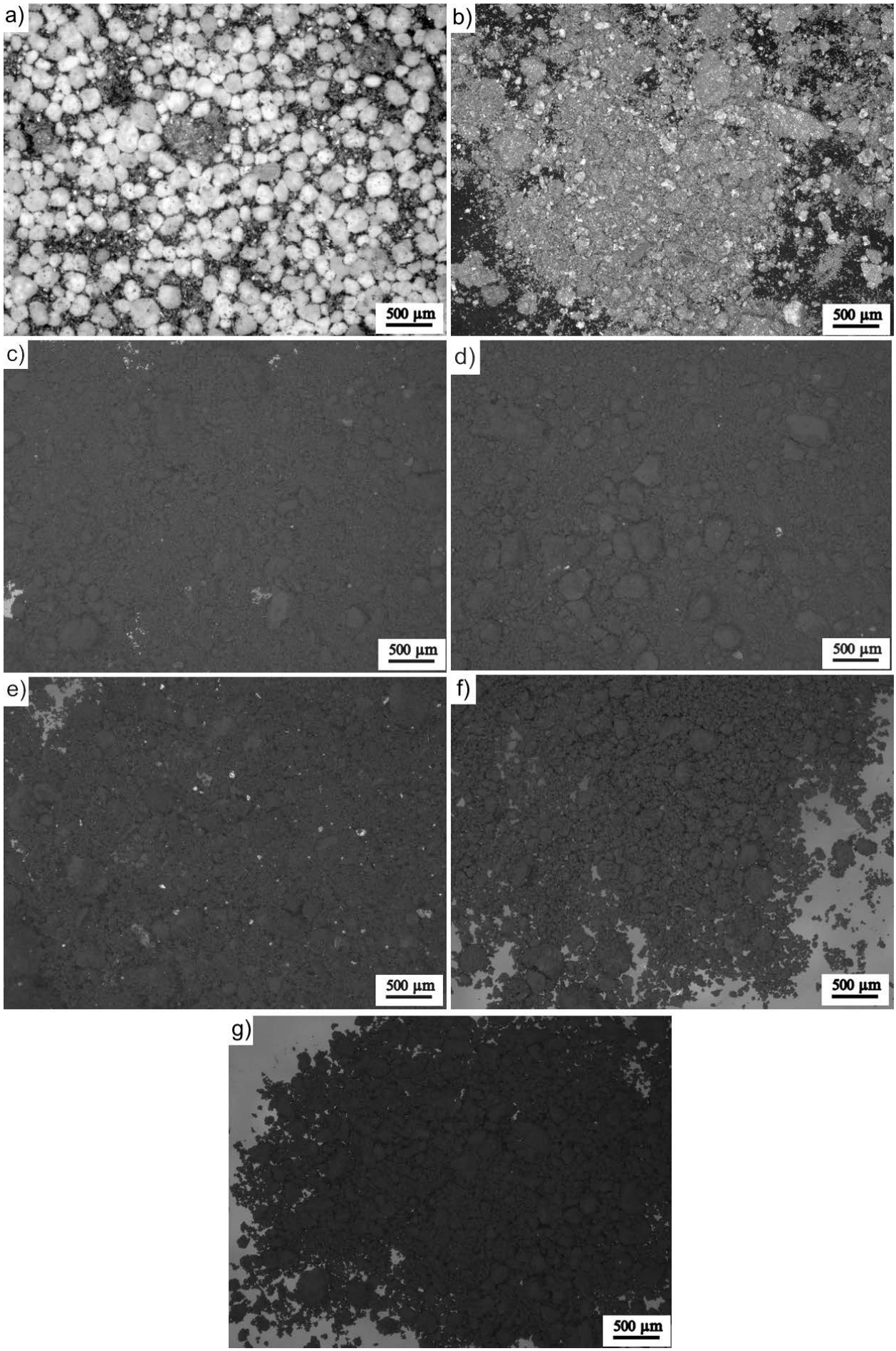

Fig. 7: SM images of the stoichiometric $HfCl_4$-B_2O_3-Mg powders: (a) as-blended, (b) MCS for 10 min, (c) MCS for 15 min, (d) MCS for 3 h, (e) MCS for 5 h, (f) MCS for 3 h and purified, (g) MCS for 3 h, purified and annealed.

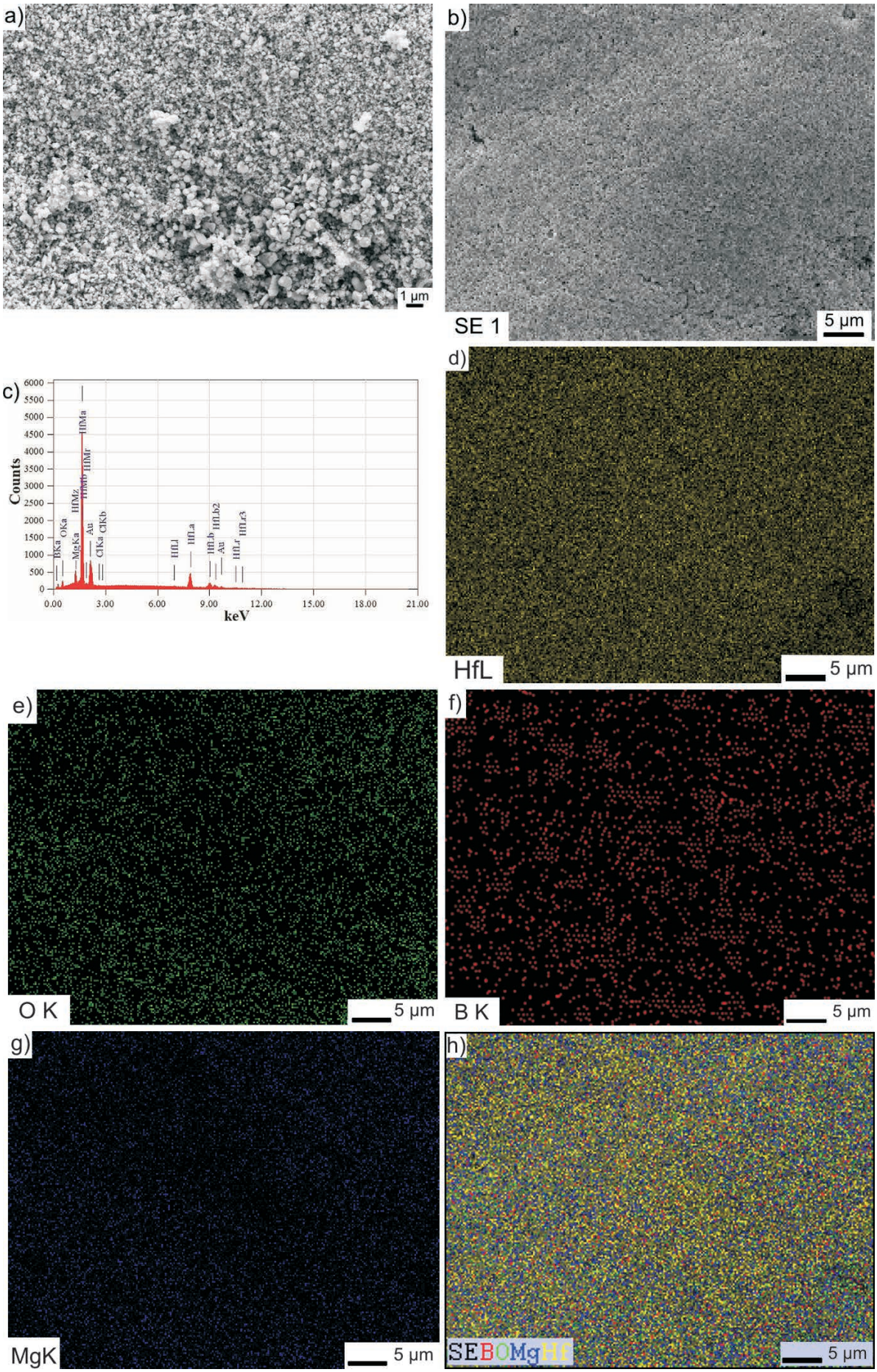

Fig. 8: SEM/EDX/EDS analyses of the stoichiometric $HfCl_4$-B_2O_3-Mg powders after mechanochemical synthesis for 3 h and subsequent purification: (a) SEM image, (b) SEM image for general EDX analysis, (c) EDX analysis, and SE elemental mappings for (d) Hf, (e) O, (f) B, (g) Mg and (h) their overlapped mapping.

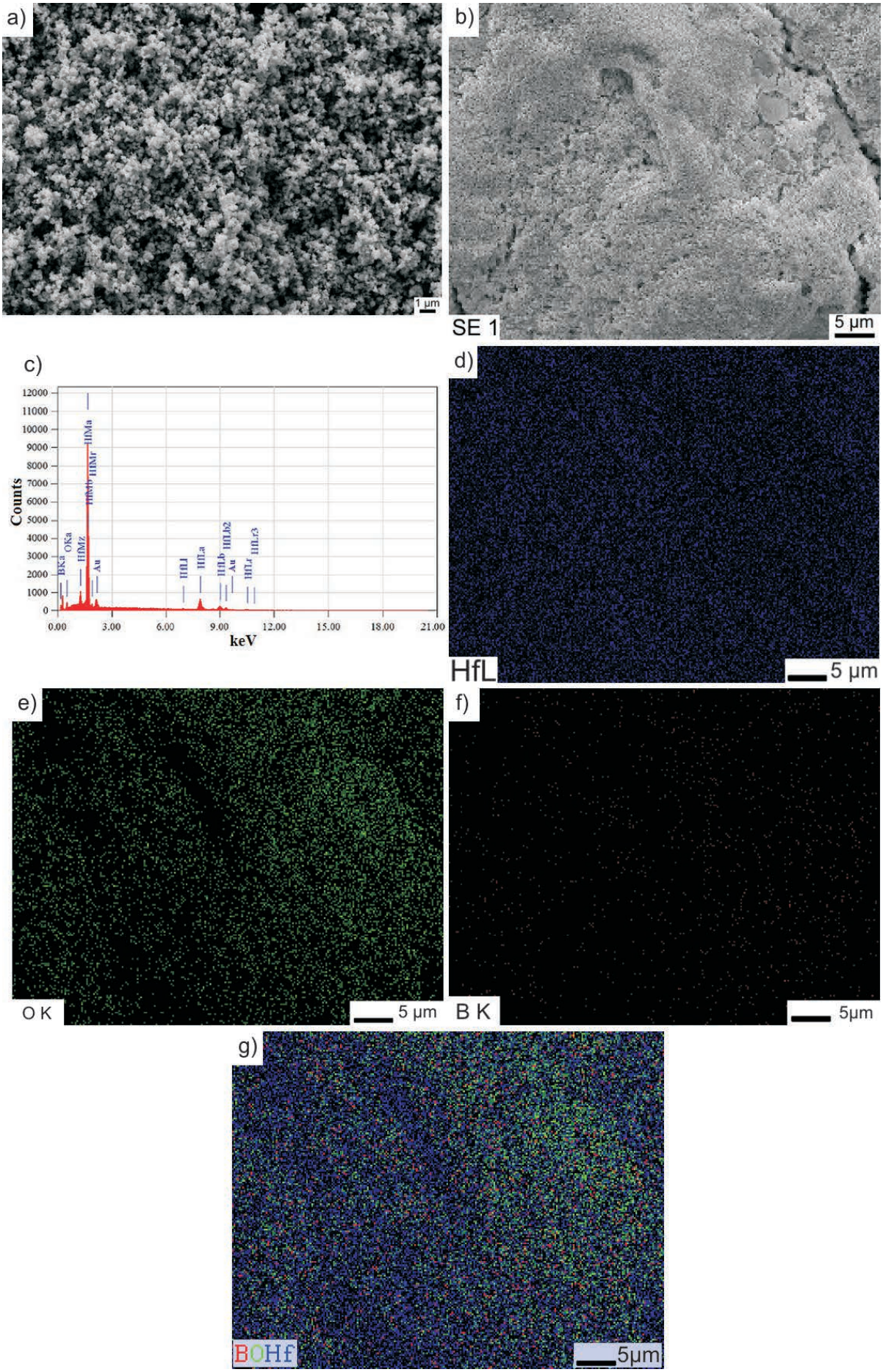

Fig. 9: SEM/EDX/EDS analyses of the stoichiometric $HfCl_4$-B_2O_3-Mg powders after mechanochemical synthesis for 3 h, purification, annealing and additional leaching: (a) SEM image, (b) SEM image for general EDX analysis, (c) EDX analysis, and SE elemental mappings for (d) Hf, (e) O, (f) B and (g) their overlapped mapping.

Furthermore, the particle size distributions of the stoichiometric $HfCl_4$-B_2O_3-Mg powders after mechanochemical synthesis at different durations (1, 3 and 5 h) and purification were investigated by using a particle size analyzer in distilled water as dispersant media. The average particle sizes of the 1-, 3- and 5-h mechanochemically synthesized and purified powders were determined as 151.4 ± 1.21, 140.0 ± 0.82 and 129.5 ± 0.76 nm, respectively. Although a slight decrease in the average particle sizes of the powders effected with the increasing MCS duration was observed, the values were close to each other. Hence, it can be asserted that the steady-state conditions were almost reached after 1 h of MCS, which was also inferred from the XRD and Rietveld analyses. XRD analyses were also utilized to determine the average crystallite sizes and lattice strains of the HfB_2 phase in the stoichiometric $HfCl_4$-B_2O_3-Mg powders (using the (001), (100) and (101) reflections) after MCS at different durations and subsequent purification (Table 2). As expected, the average crystallite sizes decreased and lattice strains increased with increasing MCS duration. Owing to the continuous mechanical deformation imposed into the powders during milling, particle and crystallite refinement occurred and the lattice strain increased [17, 45].

Table 2: Average crystallite sizes and lattice strains of the HfB_2 phase in the stoichiometric $HfCl_4$-B_2O_3-Mg powders after mechanochemical synthesis at different durations and subsequent purification.

MCS Duration (h)	Crystallite Size (nm)	Lattice Strain (%)
1 h	84.0 ± 2.60	0.385 ± 0.008
3 h	66.9 ± 1.85	0.495 ± 0.012
5 h	39.4 ± 1.40	0.884 ± 0.016

The secondary electron SEM images and particle size distribution graph of the powders after 3 h of MCS, purification, annealing and additional HCl leaching are shown in Figs. 10(a) – (c), respectively. The powders have round-shaped morphology (containing particles smaller than 400 nm), similar to the powders obtained after MCS for 3 h and purification. However, there are also rectangular or angular-shaped particles. The average particle size of the powders was determined as 140.5 nm, which is also in good agreement with the observed particle size in the SEM images. Thus, the annealing treatment conducted at 1000 °C did not cause grain growth and there is only a very slight increase in the particle sizes of the powders.

To observe and identify the smaller particles that could not be analyzed by means of SEM analyses because of the agglomeration, TEM analyses were conducted on the resultant powders. Figs. 11(a) and (c) are bright-field (BF) images of the stoichiometric $HfCl_4$-B_2O_3-Mg powders after MCS for 3 h, purification, annealing and additional leaching. The BF images showed round- and angular (like rectangular or cube) particles in sizes varying between 50 and 200 nm, which is also compatible with the SEM

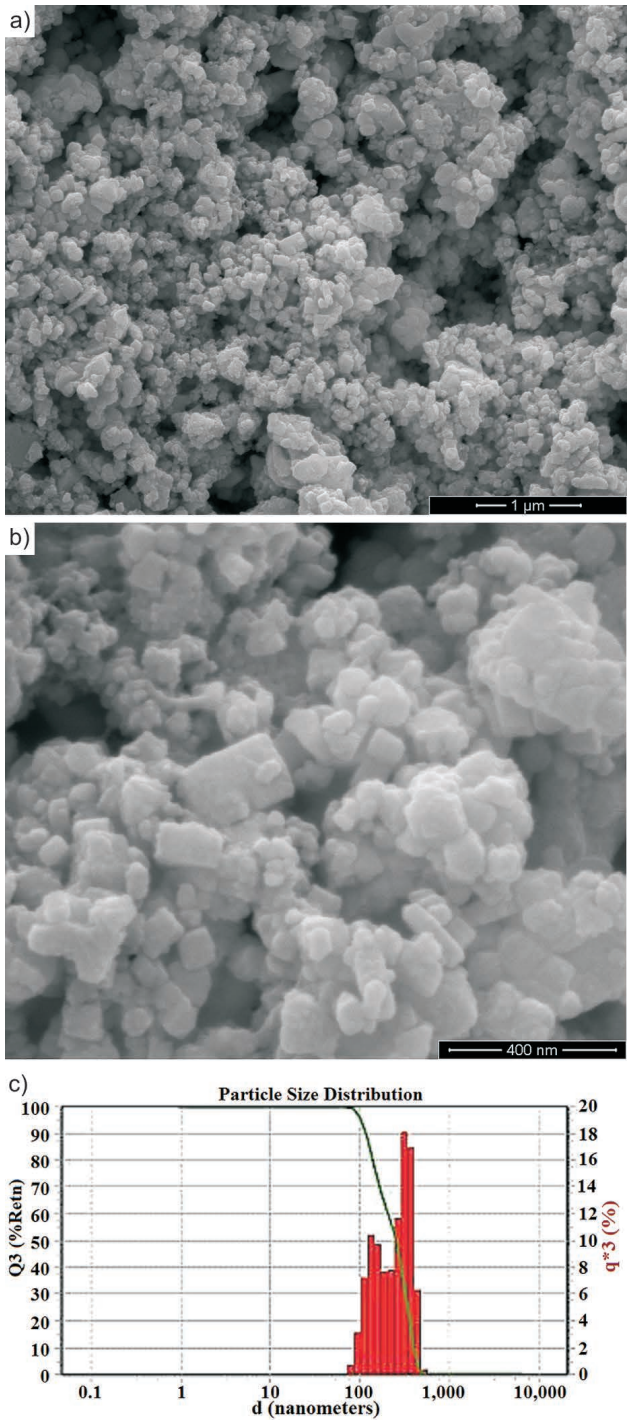

Fig. 10: Low- (a) and high-magnification (b) SEM images, and particle size distribution graph (c) of the stoichiometric $HfCl_4$-B_2O_3-Mg powders after mechanochemical synthesis for 3 h, purification, annealing and additional leaching.

and PSA results. However, there are still large agglomerates consisting of smaller particles. Figs. 11(b) and (d) are the corresponding SADPs of the white-circled regions in Figs. 11(a) and (c), respectively. They indicated the presence of the polycrystalline monoclinic HfO_2 phase and the presence of the polycrystalline hexagonal HfB_2 phase.

(4) Phase and microstructural analyses of the consolidated samples

The HfB_2-HfO_2 ceramic powders prepared with 3 h of MCS, purification, annealing and additional leaching were

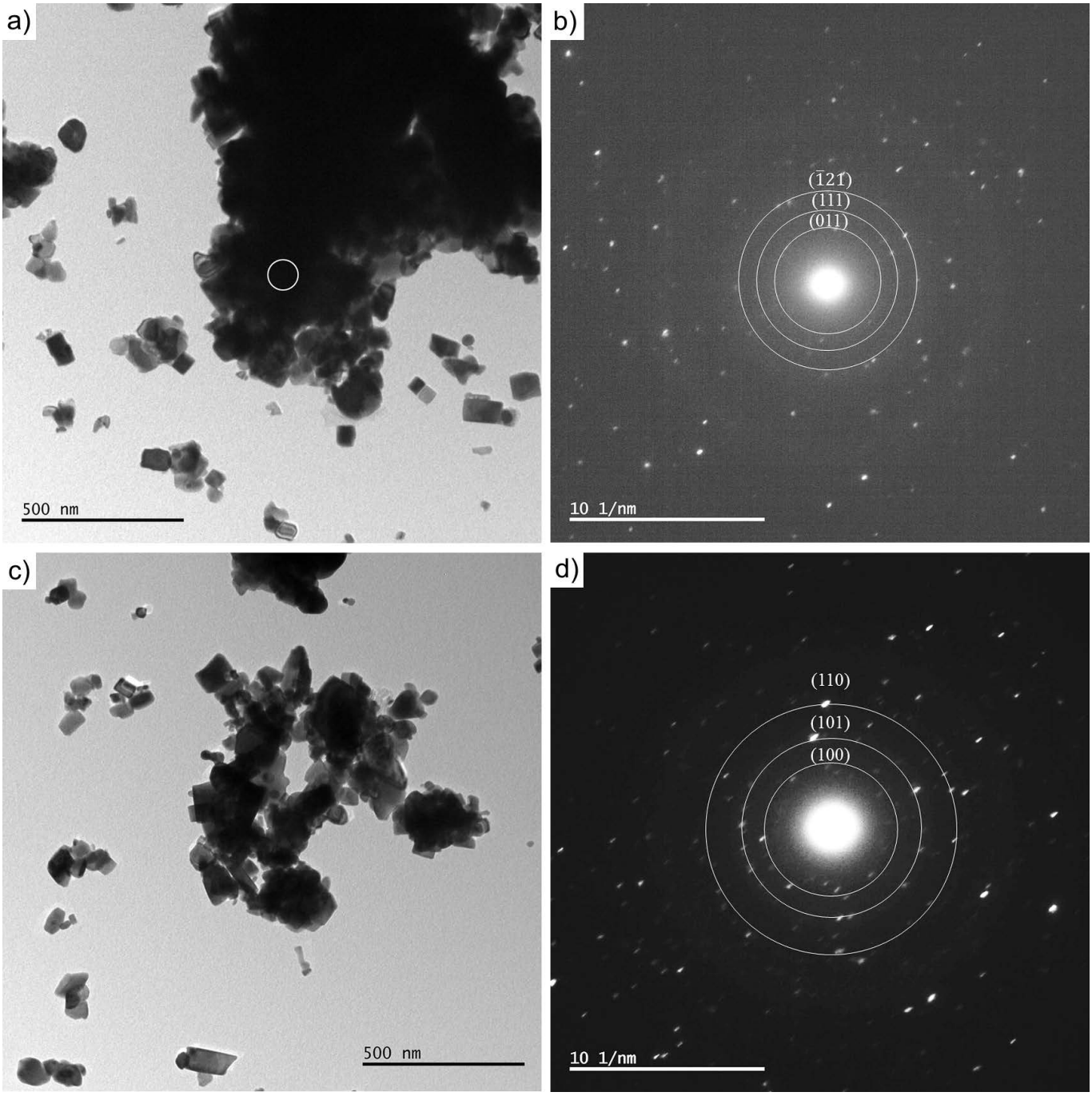

Fig. 11: TEM analyses conducted on the stoichiometric $HfCl_4$-B_2O_3-Mg powders after mechanochemical synthesis for 3 h, purification, annealing and additional leaching: (a) Bright-field (BF) TEM image, (b) corresponding selected area diffraction pattern (SADP) taken from the white-circled region in (a), revealing the presence of monoclinic HfO_2 phase, (c) BF TEM image and (d) SADP taken from the white-circled region in (c), revealing the presence of hexagonal HfB_2 phase.

consolidated by using PS (with addition of 2 wt% Co) at 1500 °C for 5 h and SPS at 1700 °C for 15 min under an applied holding pressure of 60 MPa. The XRD patterns of sintered samples consolidated by PS and SPS techniques are illustrated in Fig. 12(a) and (b), respectively. In the XRD patterns, the HfB_2 and HfO_2 phases were detected without any indication of impurity. The $Mg_2Hf_5O_{12}$ phase was not observed because of its decomposition to HfO_2 and MgO phases. The decomposition of $Mg_2Hf_5O_{12}$ phase during sintering at elevated temperature was also reported in a previous study on autoclave processing and consolidation of $HfCl_4$-B_2O_3-Mg blends [22]. Correspondingly, it was proved that the $Mg_2Zr_5O_{12}$ phase decomposed to MgO and ZrO_2 phases during hot isostatic pressing at 1100 °C [42]. The relative intensities of the three most intensive lines of HfB_2 differed significantly from the HfB_2 lines in the XRD patterns of the powder samples (Figs. 2, 3, 4 and 6). It appears somewhat misleading because diffraction info is obtained from the reflecting planes of the both submicron- and nano-scaled powders with high surface area and high strain due to the continuous deformation during mechanochemical synthesis. In general, the number of diffraction signals is proportional to the area under the highly

broadened peaks of the mechanochemically synthesized powders. After annealing of these powders and after removal of residual strain by the effect of temperature, the XRD pattern represents that of a typical bulk sample and the intensities or intensity ratios are similar to those in the ICDD cards. Owing to the fact that the XRD peaks in the sintered samples are very narrow and peak heights are taken into consideration. Similarly, an intensity difference between the powder and bulk samples of HfB_2/HfO_2 was reported in some studies [22, 23]. Secondary electron SEM images of the bulk samples consolidated with PS and SPS techniques are shown in Figs. 13(a) and (b), respectively. The microstructure of PS sample includes open porosities and indicates a lower densification rate compared to SPS sample.

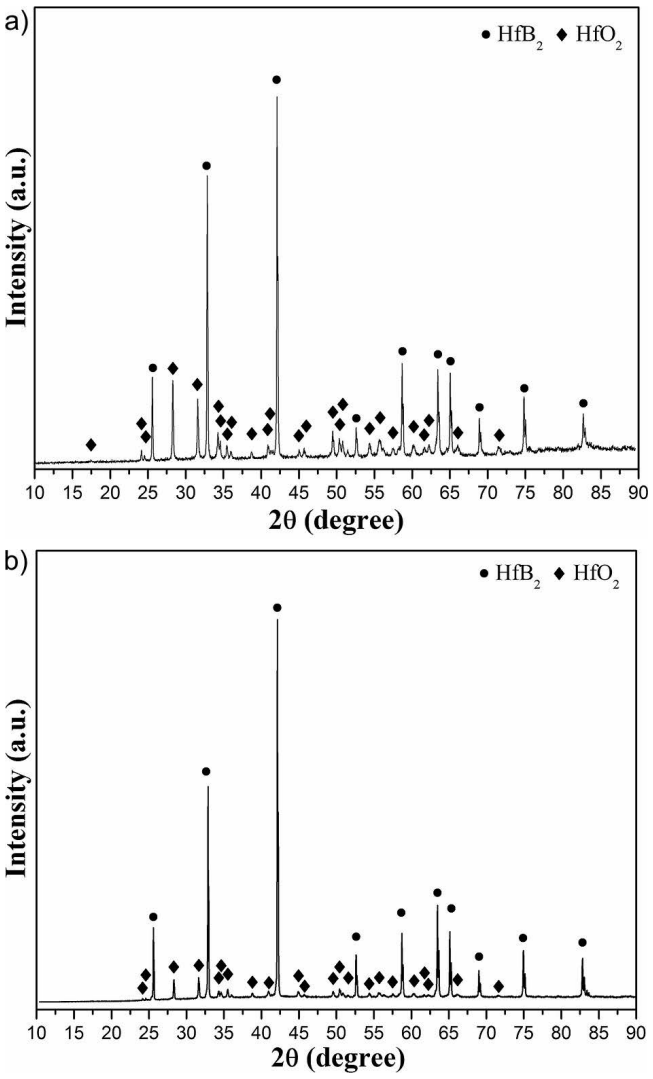

Fig. 12: XRD patterns of the bulk samples consolidated with: (a) PS and (b) SPS techniques.

(5) Mechanical properties of the consolidated samples

Table 3 shows the Archimedes and relative densities and microhardness ($HV_{0.2}$) values of the sintered samples. A relative density amount of 91.82 % was reached with the PS technique at 1500 °C for 5 h and 2 wt% Co addition. The hardness value of PS sample was determined as 14.72 GPa.

Table 3: Density and microhardness values of the bulk samples consolidated with PS and SPS techniques.

Sintering Technique	Archimedes Density (g/cm^3)	Relative Density (%)	$HV_{0.2}$ (GPa)
PS (2 wt% Co)	9.77	91.82	14.72 ± 1.49
SPS	10.00	93.79	18.45 ± 1.55

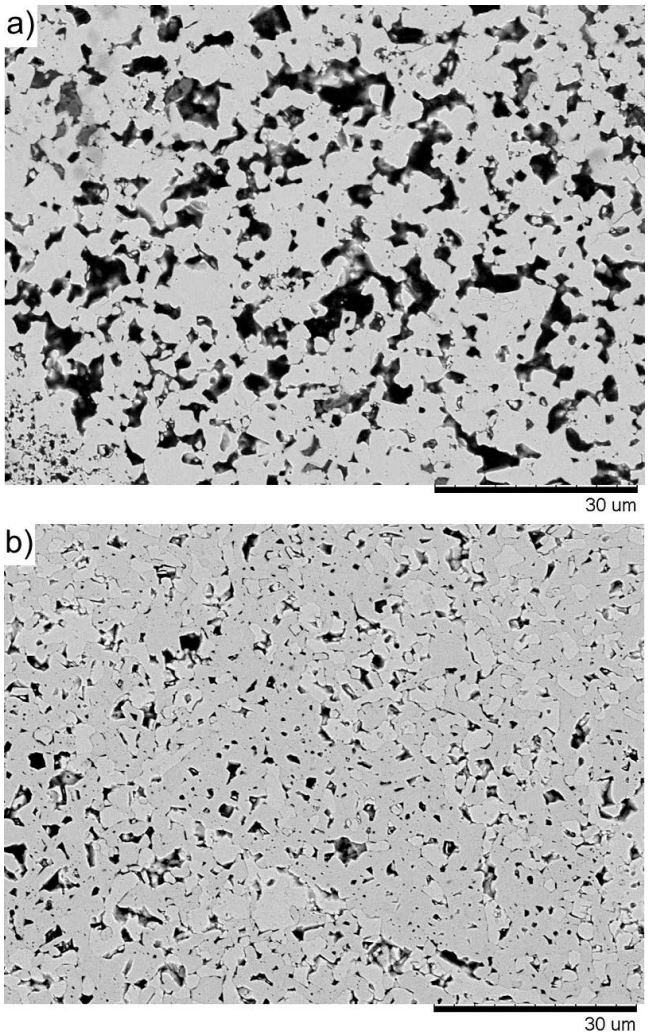

Fig. 13: SEM images of the bulk samples consolidated with: (a) PS and (b) SPS techniques.

It is very difficult to obtain high densification rates with conventional sintering techniques because of very high melting point and covalent bonding of HfB_2. Although, pressureless sintering (PS) technique has important advantages such as cost effectiveness and producing near-net shape components, to reach a reasonable densification, a high sintering temperature is often needed owing to the lack of external holding pressure. The reduced particle size and sintering additives are generally provided to compensate for these limitations. The densification rate of diborides has been appreciably increased with various additives such as refractory metals (Fe, Cr, Ni), refractory

metal silicides ($MoSi_2$, $TiSi_2$, $HfSi_2$) and ceramic additives (SiC, Si_3N_4) [9, 46, 47, 48]. Recently, sintering studies have been focused on some modern sintering techniques and sintering additives. The sintering aids such as SiC, $MoSi_2$, La_2O_3, B_4C, WC, etc. are investigated for the liquid-phase sintering of hafnium diboride [30, 47, 49]. Silvestroni *et al.* reported the fabrication of HfB_2-$MoSi_2$ composites with different amounts of $MoSi_2$ between 5 – 20 wt% by means of pressureless sintering at 1950 °C for 1 h [30]. Sintered samples including 0 and 20 wt% $MoSi_2$ reached relative density values of 89 and 98 %, respectively. The hardness of HfB_2-5$MoSi_2$ and HfB_2-20$MoSi_2$ composites was reported as about 18.2 GPa for both. Another pressureless sintering study on the HfB_2-20 vol% SiC ceramics was conducted using WC as a sintering aid at 2200 °C for 2 h, and a relative density of 99 % was reported. It was shown that the complex reactions between WC and the HfB_2-SiC system enabled the high densification rate. The HfB_2 ceramics were sintered at a temperature range of 2100 – 2350 °C with B_4C (between 0 and 2 wt%) as a sintering aid without external pressure. It was stated that the formation of a liquid phase which wetted the hafnium diboride grains effectively during the liquid-phase sintering process improved the densification. The best result for Vickers hardness recorded for the HfB_2-2 wt% B_4C sample sintered at 2150 °C was 20.1 GPa [47]. Additionally, HfB_2-HfO_2 powders consolidated by means of PS at 1700 °C for 6 h had a relative density value of 85.12 % and it was stated that the existence of HfO_2 phase had a positive effect on the densification rate [22]. A comparatively higher densification rate for HfB_2-HfO_2 powders at a lower temperature was reached in the present study with nano-sized starting particles and liquid phase sintering provided by Co addition. In another study, the relative density of bulk nanocrystalline HfB_2 (with an average particle size of 145.2 nm) sintered by means of PS with 2 wt% Co addition at 1500 °C for 5 h was reported as 90.14 % [23]. Moreover, a higher relative density value was reached by means of SPS (93.79 %) compared to the PS technique. The hardness value of the PS and SPS samples was determined as 14.72 and 18.45 GPa, respectively.

In former studies based on the SPS technique, the relative density and hardness values for HfB_2-HfO_2 (SPS at 1700 °C for 15 min) were found as 91.11 % and 15.60 GPa, while the same values for HfB_2 (SPS at 1900 °C for 15 min) were 94.18 % and 20.99 GPa, respectively [22, 23]. Moreover, the relative density and hardness values for hot-pressed (at 2200 °C for 60 min under 30 MPa) HfB_2-20 vol% SiC powders with 10 μm average particle size were 93.8 % and 18.3 ± 0.5 GPa, respectively [50]. Additionally, the relative density and hardness values for HfB_2-15 vol% $MoSi_2$ (particle size 0.5 – 5 μm, SPS at 1750 °C) were determined as 94.7 % and 15.7 ± 0.8 GPa, respectively[51]. Besides, it was stated that $MoSi_2$ has a low hardness (~ 9 GPa) and its addition decreased the hardness of either ZrB_2 or HfB_2-based ceramics [9]. In addition, HfB_2-SiC composites were prepared by means of the reactive spark plasma sintering (RSPS) technique. $HfSi_2$, B_4C and carbon black powders were mixed in stoichiometric composition and sintered in a spark plasma sintering apparatus at 1600 °C under a pressure of 40 MPa for 10 min [36]. It was claimed the HfB_2 and SiC phases were distributed homogeneously in the structure and their particle sizes were 2 and 1 μm, respectively. The relative density of the products was 98.7 %, and the hardness of composites was 20.4 GPa. The particle size reduction (obtained by ball milling of the starting powders) and the enhanced mass transfer rates were stated as critical factors for reaching the high densification rates during the reactive SPS [36].

SEM images of the surfaces of the PS and SPS samples after they had been subjected to sliding wear tests are shown in Fig. 14(a) and (b), respectively. Distinguishable macroholes due to the loss of material from the surface during sliding and some cracks are clearly seen in the SEM image of the PS sample (Fig. 14(a)). However, sliding test caused less wear and damage on the surface of the SPS sample in Fig. 14(b) in connection with its higher relative density and microhardness. The wear volume loss and friction coefficient values of the consolidated samples are shown in Table 4. Fig. 14(c) shows the wear profile of the consolidated samples in comparison. The respective volume loss from the surfaces of the PS and SPS samples was found to be 7.39×10^{-3} and 4.30×10^{-3} mm^3. Hence, higher wear volume loss amount for the PS sample is observed in the wear profile, which is clearly compatible with the SEM images in Figs. 14(a) and (b). In a previous study on the sliding wear tests of HfB_2-HfO_2 composites consolidated by means of PS (at 1500 °C for 5 h) and SPS (at 1700 °C for 15 min) techniques, volume loss amounts were reported as 13.69×10^{-3} and 5.539×10^{-3} mm^3, respectively [22]. In addition, the friction coefficient of the pressureless-sintered sample sliding against an alumina counterface is 0.54 and a slightly higher friction coefficient value of 0.60 is observed for the spark-plasma-sintered sample. Chakraborty *et al.* determined the friction coefficients of ZrB_2-TiB_2 (with TiB_2 up to 30 wt%) samples in the range of 0.31 – 0.532 [52]. Additionally, the friction coefficient values of vanadium and niobium borides sintered by means of SPS were reported as between 0.49 and 0.53 [35]. Therefore, it can be said that the friction values of the PS and SPS samples were close to the reported values in the literature and compatible with each other.

Table 4: Wear volume loss and friction coefficient values of the bulk samples consolidated with PS and SPS techniques.

Sintering Technique	Wear Volume Loss (mm^3)	Friction Coefficient
PS (2 wt% Co)	7.39×10^{-3}	0.54
SPS	4.30×10^{-3}	0.60

Consequently, HfB_2-HfO_2 ceramic powders and their consolidated samples were prepared by means of mechanochemical synthesis, annealing and purification treatments. MCS provided a simple way for synthesizing HfB_2-HfO_2 powders from economical raw materials at room temperature. On the basis of the powder and bulk characterizations conducted in the present study, it can be stated that the utilized methods can open up an alternative

path for obtaining pure HfB_2-HfO_2 products as candidate structural materials.

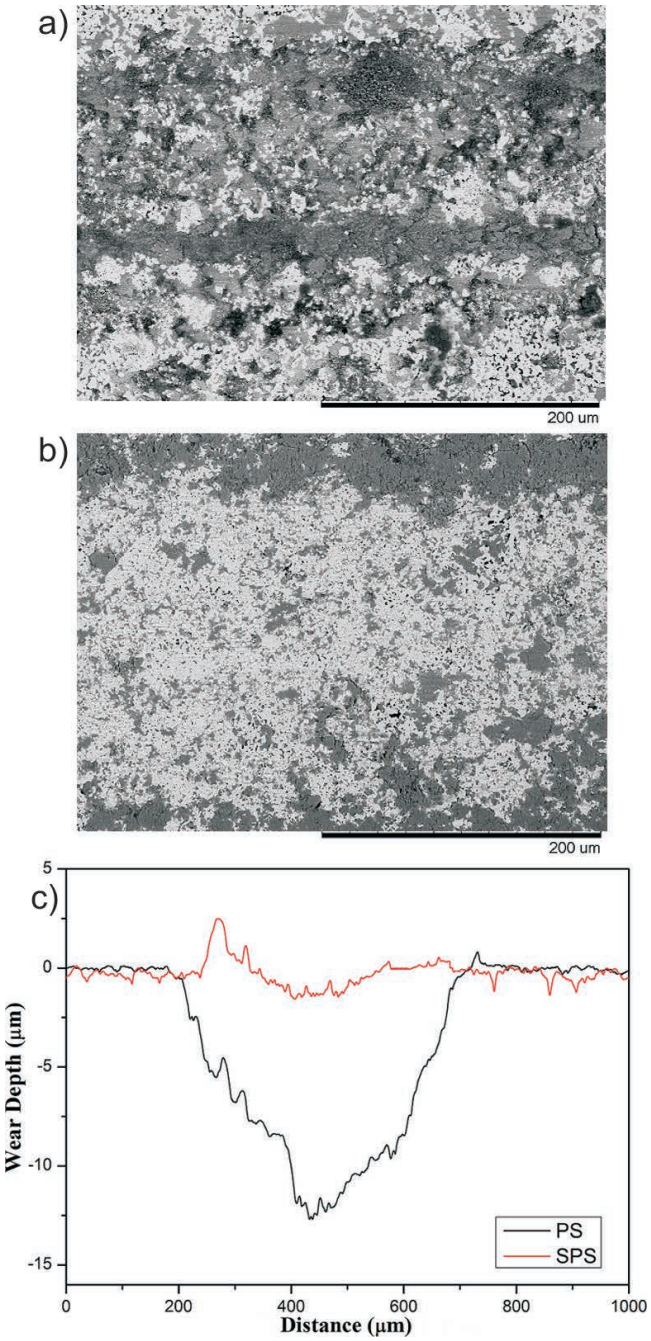

Fig. 14: Worn surface SEM images of the bulk samples consolidated with: (a) PS (with 2 wt% Co), (b) SPS techniques, and (c) their corresponding wear profiles.

IV. Conclusions

This study reports on the *in-situ* synthesis of nanostructured HfB_2-HfO_2 composite powders and their subsequent consolidation process. The significant results of mechanochemical synthesis, annealing, leaching and the consolidation processes can be summarized as follows:

- After mechanochemical reaction of $HfCl_4$-B_2O_3-Mg blends for 3 h and subsequent washing and 4 M-HCl-leaching treatments, the HfB_2-HfO_2 composite powders were obtained with the presence of a very small amount of $Mg_2Hf_5O_{12}$ phase.
- It was determined that the $Mg_2Hf_5O_{12}$ is not stable over 1000 °C and it decomposed to MgO and HfO_2 phases.
- The HfB_2-HfO_2 powders obtained after mechanochemical synthesis, annealing and purification processes had an average particle size of 140 nm and predominantly round- and angular-shaped morphology.
- The relative density values of HfB_2-HfO_2 composites obtained by means of PS (with 2 wt% Co) and SPS techniques were 91.82 % and 93.79 %, respectively. A higher densification rate for HfB_2-HfO_2 ceramic was achieved compared to that in the literature with a Co sintering aid. Thus, it can be said that metallic Co is a promising sintering aid for HfB_2-based ceramics and it deserves further research.
- A higher hardness value for the SPS sample was obtained at 18.45 GPa compared to the PS sample (14.72 GPa) in accordance with their densification rates. In addition, wear volume loss amount and friction coefficient values of the SPS samples were measured as 4.30 mm^3 and 0.60, respectively.

Acknowledgements

This study was financially supported by "The Scientific and Technological Research Council of Turkey (TÜBİTAK)" with the project number of 112M470 and by "Istanbul Technical University Scientific Research Projects" with the project number of 37544. The authors also wish to express their appreciation to Prof. Dr Servet Turan for his help with the SPS experiments and Prof. Dr Hüseyin Çimenoğlu and M.Sc. Faiz Muhaffel for their support in the wear tests.

References

1 Rapp, B.: Materials for extreme environments: Defense, aviation, and space agencies are beginning to look at the advanced composite materials necessary for hypersonic speeds, *Mater. Today*, **9**, [6], (2006).

2 Orru, R., Cao, G.: Comparison of reactive and non-reactive spark plasma sintering routes for the fabrication of monolithic and composite ultra high temperature ceramics (UHTC) materials, *Materials*, **6**, 1566 – 1583, (2013).

3 Cincotti, A., Licheri, R., Locci, A.M., Orru, R., Cao, G.: A review on combustion synthesis of novel materials: recent experimental and modeling results, *J. Chem. Technol. Biot.*, **78**, 122 – 127, (2003).

4 Zhang, X., Li, W., Hong, C., Han, W.: Microstructure and mechanical properties of ZrB_2 based composites reinforced and toughened by zirconia, Int. J. Appl. Ceram. Tec., 5, 499 – 504, (2008).

5 Basu, B., Vleugels, J., Biest, O.: Development of ZrO_2-ZrB_2 composites, *J. Alloy. Compd.*, **334**, 200 – 204, (2001).

6 Balcı, Ö., Ağaoğulları, D., Duman, İ., Öveçoğlu, M.L.: Carbothermal production of ZrB_2-ZrO_2 ceramic powders from ZrO_2-B_2O_3/B system by high-energy ball milling and annealing assisted process, *Ceram. Int.*, **38**, 2201 – 2207, (2012).

7 Huang, F., Yan, A., Fu, Z., Yin, S., Zhang, F., Qiang, Y.: Self-assembled synthesis of TiO_2/TiB_2 nanowall and its photocatalytic properties, *J. Alloy. Compd.*, **574**, 49 – 53, (2013).

8 Huang, F., Fu, Z., Yan, A., Wang, W., Wang, H., Wang, Y., Zhang, Q.: Several shape-controlled TiO_2/TiB_2 hybrid materials with a combined growth mechanism, *Mater. Lett.*, **63**, 2655 – 2658, (2009).

[9] Fahrenholtz, W.G., Hilmas, G.E., Talmy, I.G., Zaykoski, J.A.: Refractory diborides of zirconium and hafnium, *J. Am. Ceram. Soc.*, **90**, 1347 – 1364, (2007).

[10] Opeka, M.M., Talmy, I.G., Wuchina, E.J., Zaykoski, J.A., Causey, S.J.: Mechanical, thermal, and oxidation properties of refractory hafnium and zirconium compounds, *J. Eur. Ceram. Soc.*, **19**, 2405 – 2414, (1999).

[11] Wang, J., Li, H.P., Stevens, R.: Hafnia and hafnia-toughened ceramics, *J. Mater. Sci., 27, 5397 – 5430, (1992).*

[12] Kumar, H.P., Vidya, S., Kumar, S.S., Vijayakumar, C., Solomon, S., Thomas, J.K.: Optical properties of nanocrystalline HfO_2 synthesized by an auto-igniting combustion synthesis, *J. Asian Ceram. Soc.*, **3**, 64 – 69, (2015).

[13] Toraya, H., Yoshimura, M., Somiya, S.: Hydrothermal reaction-sintering of monoclinic HfO_2, *J. Am. Ceram. Soc.*, **65**, 159 – 160, (1982).

[14] Ramadoss, A., Krishnamoorthy, K., Kim, S.J.: Facile synthesis of hafnium oxide nanoparticles via precipitation method, *Mater. Lett.,* **75**, 215 – 217, (2012).

[15] Paul, A., Jayaseelan, D.D., Venugopal, S., Zapata-Solvas, E., Binner, J.G.P., Vaidhyanathan, B., Lee, W.E.: UHTC composites for hypersonic applications, *Am. Ceram. Soc. Bull.*, **91**, 22 – 28, (2012)

[16] Ni, D.W., Zhang, G.J., Kan, Y.M., Wang, P.L.: Synthesis of monodispersed fine hafnium diboride powders using carbo/borothermal reduction of hafnium dioxide, *J. Eur. Ceram. Soc.*, **91**, 2709 – 2712, (2008).

[17] Suryanarayana, C.: Mechanical alloying and milling, *Prog. Mater. Sci.*, **46**, 1 – 184, (2001).

[18] Bateni, A., Repp, S., Thomann, R., Acar, S., Erdem, E., Somer, M.: Defect structure of ultrafine MgB_2 nanoparticles, *Appl. Phys. Lett.*, **105**, 202605, (2014).

[19] Genc, R., Alas, M.O., Harputlu, E., Repp, S., Kremer, N., Castellano, M., Colak, S.G., Ocakoglu, K., Erdem, E.: High-capacitance hybrid supercapacitor based on multi-colored fluorescent carbon-dots, *Sci. Reports*, **7**, 11222, (2017).

[20] Erdem, E., Semmelhack, H.C., Bottcher, R., Rumpf, H., Banys, J., Matthes, A., Glasel, H.J., Hirsch, D., Hartmann, E.: Study of the tetragonal-to-cubic phase transition in Pb-TiO_3 nanopowders, *J. Phys.-Condens. Mat.*, **18**, 3861 – 3874, (2006).

[21] Akçamlı, A., Ağaoğulları, D., Balcı, Ö., Öveçoglu, M.L., Duman, İ.: Synthesis of HfB_2 powders by mechanically activated borothermal reduction of $HfCl_4$, *Ceram. Int.*, **42**, 3797 – 3807, (2016).

[22] Akçamlı, N., Ağaoğulları, D., Balcı, Ö., Öveçoğlu, M.L., Duman, İ.: Mechanical activation-assisted autoclave processing and sintering of HfB_2-HfO_2 ceramic powders, *Ceram. Int.*, **42**, 14642 – 14655, (2016).

[23] Akçamlı, N., Ağaoğulları, D., Balcı, Ö., Öveçoğlu, M.L., Duman, İ.: Synthesis of bulk nanocrystalline HfB_2 from $HfCl_4$-$NaBH_4$-Mg ternary system, *J. Mater. Sci.*, **52**, 12689 – 12705, (2017).

[24] Chen, L., Gu, Y., Shi, L., Yang, Z., Ma, J., Qian, Y.: Synthesis and oxidation of nanocrystalline HfB_2, *J. Alloy Compd.*, **368**, 353 – 356, (2004).

[25] Kravchenko, S.E., Burlakova, A.G., Korobov, I.I.: Preparation of hafnium diboride nanopowders in an anhydrous $Na_2B_4O_7$ ionic melt, *Inorg. Mater.,* **51**, 380 – 383, (2015).

[26] Li, W., Zhang, X., Hong, C., Han, W., Han, J.: Preparation, microstructure and mechanical properties of ZrB_2-ZrO_2 ceramics, *J. Eur. Ceram. Soc.*, **29**, 779 – 786, (2009).

[27] Kiisk, V., Lange, S., Utt, K., Tätte, T., Mändar, H., Sildos, I.: Photoluminescence of sol-gel-prepared hafnia, *Physica B*, **405**, 758 – 762, (2010).

[28] Pavasupree, S., Suzuki, Y., Pivsa-Art, S., Yoshikawa, S.: Preparation and characterization of mesoporous MO_2 (M= Ti, Ce, Zr, and Hf) nanopowders by a modified sol-gel method, *Ceram. Int.*, **31**, 959 – 963, (2005).

[29] Tang, W.T., Ying, Z.F., Hu, Z., Li, W.W., Sun, J., Xu, N., Wu, J.D.: Synthesis and characterization of HfO_2 and ZrO_2 thin films deposited by plasma assisted reactive pulsed laser deposition at low temperature, *Thin Solid Films*, **518**, 5442 – 5446, (2010).

[30] Yoshimura, M., Somiya, S.: Hydrothermal synthesis of crystallized nano-particles of rare earth-doped zirconia and hafnia, *Mater. Chem. Phys.*, **61**, 1 – 8, (1999).

[31] Meskin, P.E., Sharikov, F.Y., Ivanov, V.K., Churagulov. B.R., Tretyakov. Y.D.: Rapid formation of nanocrystalline HfO_2 powders from amorphous hafnium hydroxide under ultrasonically assisted hydrothermal treatment, *Mater. Chem. Phys.*, **104**, 439 – 443, (2007).

[32] Telle, R., Sigl, L.S., Takagi. K.: Boride-based hard materials. In: Handbook of ceramic hard materials. Wiley, Weinheim, 2000.

[33] Silvestroni, L., Sciti, D.: Effects of $MoSi_2$ additions on the properties of Hf- and Zr-B_2 composites produced by pressureless sintering, *Scr. Mater.*, **57**, 165 – 168, (2007).

[34] Wang, H., Lee, S.H., Kim, H.D.: Nano-hafnium diboride powders synthesized using a spark plasma sintering apparatus, *J. Am. Ceram. Soc.*, **95**, 1493 – 1496, (2012).

[35] Balcı, Ö., Ağaoğulları, D., Muhaffel, F., Öveçoğlu, M.L., Çimenoğlu, H., Duman, İ.: Effect of sintering techniques on the microstructure and mechanical properties of niobium borides, *J. Eur. Ceram. Soc.*, **36**, 3113 – 3123, (2016).

[36] Wang, H., Lee, S.H., Feng, L.: HfB_2-SiC composite prepared by reactive spark plasma sintering, *Ceram. Int.*, **40**, 11009 – 11013, (2014).

[37] Venugopal, S., Boakye, E.E., Paul, A., Keller, K., Mogilevsky, P., Vaidhyanathan, B., Binner, J.G.P., Katz, A., Brown, P.M.: Sol-gel synthesis and formation mechanism of ultra high temperature ceramic HfB_2, *J. Am. Ceram. Soc.*, **97**, 1 – 8, (2013).

[38] Barraud, E., Bégin-Colin, S., Le Caër, G., Villieras, F., Barres, O.: Thermal decomposition of $HfCl_4$ as a function of its hydration state, *J. Solid State Chem.*, **179**, 1842 – 1851, (2006).

[39] Nyquist, R.A., Kagel, R.O.: Handbook of Infrared and Raman Spectra of Inorganic Compounds and Organic Salts. In: Infrared Spectra of Inorganic Compounds (3800 – 45 cm^{-1}). Academic Press, New York, 1971.

[40] Xia, S., Xing, P., Gao, S.: Studies on the basic compounds of magnesia cement: the thermal behaviour of magnesium oxychlorides, *Thermochim. Acta*, **183**, 349 – 363, (1991).

[41] Wu, K., Jin, Z.: Thermodynamic assessment of the HfO_2-MgO system, *Calphad*, **21**, 411 – 420, (1997).

[42] Samad, A.A., Lugscheider, E., Bobzin, K., Maes, M.: The influence of post heat treatment processes on thermal fatigue resistance of thermally sprayed coatings. In: Thermal Spray 2004: Advances in technology and tpplications. ASM International, Osaka, Japan, 2004.

[43] Ağaogulları, D., Öveçoğlu, M.L., Duman, İ.: Synthesis of LaB_6 powders from La_2O_3, B_2O_3 and Mg blends via a mechanochemical route, *Ceram. Int.*, **38**, 6203 – 6214, (2012).

[44] Lok, J.Y., Logan, K.V., Payyapilly, J.J.: Acid leaching of SHS produced magnesium oxide/titanium diboride, *J. Am. Ceram. Soc.*, **92**, 26 – 31, (2009).

[45] El-Eskandarany, M.S.: Mechanical Alloying for Fabrication of Advanced Engineering Materials. N.Y: Noyes Publications, Norwich, 2001.

[46] Sonber, J.K., Murthy, T.C., Subramanian, C., Kumar, S., Fotedar, R.K., Suri, A.K.: Investigations on synthesis of HfB_2 and development of a new composite with $TiSi_2$, *Int. J. Refract. Met. Hard. Mater.,* **28**, 201 – 210, (2010).

[47] Zou, J., Zhang, G.J., Kan, Y.M.: Pressureless densification and mechanical properties of hafnium diboride doped with B_4C: from solid state sintering to liquid phase sintering, *J. Eur. Ceram. Soc.*, **30**, 2699 – 2705, (2010).

[48] Monteverde, F.: Ultra-high temperature HfB_2-SiC ceramics consolidated by hot-pressing and spark plasma sintering, *J. Alloy. Compd.*, **428**, 197 – 205, (2007).

[49] Ni, D.W., Liu, J.X., Zhang, G.J.: Pressureless sintering of HfB_2-SiC ceramics doped with WC, *J. Eur. Ceram. Soc.*, **32**, 3627 – 363, (2012).

[50] Weng, L., Zhang, X., Han, W., Han, J.: Fabrication and evaluation on thermal stability of hafnium diboride matrix composite at severe oxidation condition, *Int. J. Refract. Met. Hard Mater.,* **27**, 711 – 717, (2009).

[51] Sciti, D., Silvestroni, L., Bellosi, A.: Fabrication and properties of HfB_2-$MoSi_2$ composites produced by hot pressing and spark plasma sintering, *J. Mater. Res.*, **21**, 1460 – 1466, (2006).

[52] Chakraborty, S., Debnath, D., Mallick, A.R., Das, P.K.: Mechanical and thermal properties of hot pressed ZrB_2 system with TiB_2, *Int. J. Refract. Met. Hard Mater.,* **46**, 35 – 42, (2014).